Catalysis Science & Technology

ROYAL SOCIETY OF CHEMISTRY

PAPER

View Article Online
View Journal | View Issue

Cite this: *Catal. Sci. Technol.*, 2025, **15**, 1839

Optimized Ru catalysts for the selective cleavage of C_{Ar}–OCH_3 bonds in guaiacol under mild conditions†

Chuqiao Song,[a] Wei Cheng,[a] Xiaojie Wu,[a] Shufang Zhao,*[ab] Ying Tang,[a] Xin Tang,[a] Yao Xu,[c] Lili Lin *[ab] and Siyu Yao *[d]

Received 21st October 2024,
Accepted 5th February 2025

DOI: 10.1039/d4cy01260g

rsc.li/catalysis

The one-pot hydrodeoxygenation of lignin-derived (alkyl)-guaiacols to (alkyl)-cyclohexanols with high selectivity is an attractive process for biomass conversion. However, designing catalysts that preferentially cleave etheric C_{Ar}–O(R) bonds over hydrogenating aromatic rings under mild conditions remains a significant challenge. In this study, we explore the structure sensitivity of supported Ru catalysts with varying particle sizes (0.6–7.5 nm) and identify the optimal catalyst for selective hydrodeoxygenation. Using a catalyst with 1.5 nm Ru particles, we achieve a ~95% yield of cyclohexanol from guaiacol under relatively mild conditions (190 °C, 5 bar H_2). *In situ* DRIFTS analysis reveals that the cleavage of C_{Ar}–OCH_3 bonds occurs preferentially over aromatic ring hydrogenation on the 1.5 nm Ru particles, minimizing side reactions and enhancing cyclohexanol selectivity.

1. Introduction

Cyclohexanols are high-value chemical intermediates that are widely used in industry for producing polymers, fragrances, and pharmaceuticals.[1,2] Currently, the production of cyclohexanols mainly relies on the selective oxidation of cyclohexane or hydrogenation of phenols from fossil fuels.[3,4] It is more environmentally friendly and sustainable if cyclohexanol can be produced using biomass-derived compounds.[5,6] Guaiacol is a typical model of lignin-derived phenols. How to selectively remove excessive methoxy groups from lignin-derived phenols *via* selective hydrodeoxygenation (HDO) reaction is necessary to obtain the desired bio-cyclohexanol products.

Typically, there are two parallel routes for the conversion of guaiacol to cyclohexanol: selective cleavage of the aromatic ether C–O bond (Csp^2–OCH_3) (demethoxylation) followed by hydrogenation of the aromatic ring (path I) and hydrogenation of the aromatic ring followed by cleavage of the aliphatic ether (Csp^3–OCH_3) bond (path II).[7,8] Due to steric constraint and high stability of the Csp^3–OCH_3 bond, once the hydrogenation reaction of the aromatic ring in guaiacol occurs before C–O bond dissociation, the final product would remain as 2-methoxycyclohexanol (2-MCH) at mild temperatures.[9,10] Hence, the order of the two parallel routes of demethoxylation and aromatic ring hydrogenation in the HDO reaction of guaiacol would largely determine the selectivities to cyclohexanol and by-product 2-MCH. However, the control of route order is difficult under mild reaction conditions due to the lower energy barrier of C=C bond hydrogenation. Therefore, designing a catalyst with both remarkable HDO activity and preferential demethoxylation over the hydrogenation of the aromatic ring ($r_{C_{Ar}-OCH_3} > r_{C_{Ar}=C_{Ar}}$) is the key to prepare cyclohexanol selectively.[11]

Noble active metals, such as Pd, Pt, Ru, Rh and Au, have been developed for facilitating guaiacol HDO under mild reaction conditions.[8,12–16] However, surfaces of Pt, Pd and Rh always interact strongly with C=C bonds, resulting in a faster aromatic ring hydrogenation.[17] In contrast, Ru with moderate oxophilicity can effectively lower the energy barrier for direct C–O bond cleavage, which is more conducive to the generation of cyclohexanol through selective cleavage of the Csp^2–OCH_3 bond followed by hydrogenation of the aromatic ring (path I).[5,8,18–20] Even so, increasing the $r_{C_{Ar}-OCH_3}/r_{C_{Ar}=C_{Ar}}$ ratio on Ru-based catalysts to further improve selectivity for cyclohexanol (usually <80%) is an important issue under

[a] *Institute of Industrial Catalysis, State Key Laboratory of Green Chemistry Synthesis Technology, College of Chemical Engineering, Zhejiang University of Technology, Hangzhou, Zhejiang 310014, China. E-mail: zhaoshufang@zjut.edu.cn, linll@zjut.edu.cn*

[b] *Zhejiang Carbon Neutral Innovation Institute & Zhejiang International Cooperation Base for Science and Technology on Carbon Emission Reduction and Monitoring, Zhejiang University of Technology, Hangzhou 310014, China*

[c] *Beijing National Laboratory for Molecular Sciences, College of Chemistry and Molecular Engineering and College of Engineering and BIC-ESAT Peking University, Beijing 100871, China*

[d] *Key Laboratory of Biomass Chemical Engineering of Ministry of Education, College of Chemical and Biological Engineering, Zhejiang University, Hangzhou, 310027, China. E-mail: yaosiyu@zju.edu.cn*

† Electronic supplementary information (ESI) available. See DOI: https://doi.org/10.1039/d4cy01260g

relatively mild conditions.[21] It has been recognized that the hydrogenation of the aromatic ring prefers relatively large metal domains (~6 metal atoms),[22,23] which makes it sensitive to particle size, while smaller Ru aggregates could mediate the demanding C–O bond cleavage.[24–26] Therefore, there should be an optimal Ru particle size in regulating the $r_{C_{Ar}-OCH_3}/r_{C_{Ar}=C_{Ar}}$ ratio in guaiacol HDO.[27] By controlling the Ru particle size, the geometrical structure can be optimized by influencing the concentration of various surface sites to obtain higher HDO activity and cyclohexanol selectivity.[28,29]

Herein, we reported that 1.5 nm Ru particles supported on inert γ-Al_2O_3 ($Ru_{1.5}$/γ-Al_2O_3) display the best product selectivity to cyclohexanol from guaiacol among all the well-prepared Ru clusters and particles ($Ru_{0.6}$/γ-Al_2O_3, $Ru_{1.5}$/γ-Al_2O_3, $Ru_{2.5}$/γ-Al_2O_3, and $Ru_{7.5}$/γ-Al_2O_3 catalysts). Under optimal conditions, ~95% selectivity to cyclohexanol and ~99% conversion of guaiacol were achieved over $Ru_{1.5}$/γ-Al_2O_3 within 6 h. Kinetic studies showed that decreasing the Ru particle size improves the Csp^2–OCH_3 bond cleavage priority and the selectivity to products from path I (cyclohexanol, cyclohexanone, and phenol). At the same time, it greatly inhibits undesirable aromatic ring hydrogenation before C–O dissociation which leads to the formation of 2-MCH from path II (aromatic ring hydrogenation). *In situ* diffuse reflectance infrared Fourier transform spectroscopy (DRIFTS) showed that Csp^2–OCH_3 bond cleavage occurs preferentially than hydrogenation of the aromatic ring in guaiacol on the $Ru_{1.5}$/γ-Al_2O_3 catalyst. CO-DRIFTS and quasi-*in situ* XPS confirm the existence of different Ru sites on Ru/γ-Al_2O_3 catalysts, and the proportion of different surface sites could be controlled by regulating particle sizes. Mechanism studies imply that the Csp^2–OCH_3 cleavage step preferentially occurred at the low coordinated Ru sites, while the hydrogenation of aromatic rings preferentially occurred at the coordination saturated sites of Ru NPs. The optimized $Ru_{1.5}$/γ-Al_2O_3 catalyst also shows good selectivity in the synthesis of cyclohexanol derivatives by the hydrodeoxygenation of lignin-derived phenolic compounds.

2. Experimental section

2.1 Materials

Ruthenium trichloride (≥99.5%, Shanghai Titan Technology Co., Ltd.), γ-Al_2O_3 (99.99%, Hangzhou Shuangmu Chemical Co., Ltd.), $NaBH_4$ (98%, Sinopharm Chemical Reagent Co., Ltd.), ethanol (AR, Sinopharm Chemical Reagent Co., Ltd.), sodium citrate (98%, Sinopharm Chemical Reagent Co., Ltd.) Na_2CO_3 (99.5%, Shanghai Aladdin Biochemical Technology Co., Ltd.), $RuNO(NO_3)_3$ (99%, Shanghai Macklin Biochemical Technology Co., Ltd.), urea (99%, Tokyo Huacheng Industrial Co., Ltd.), guaiacol (99%, Shanghai Macklin Biochemical Technology Co., Ltd.), cyclohexanone (99%, Sinopharm Chemical Reagent Co., Ltd.), phenol (99.5%, Shanghai Yien Chemical Technology Co., Ltd.), 2-methoxycyclohexanol (2-MCH, 95%, Wuhan Kamik Technology Co., Ltd.), 3-methoxyphenol (97%, Shanghai Haohong Biomedical Technology Co., Ltd.), 4-methoxyphenol (98%, Shanghai Bide Pharmaceutical Technology Co., Ltd.), 2-methoxy-4-methylphenol (98%, Shanghai Haohong Biomedical Technology Co., Ltd.), 2-methoxy-4-ethylphenol (95%, Shanghai Haohong Biomedical Technology Co., Ltd.), 2-methoxy-4-propylphenol (98%, Shanghai Bide Pharmaceutical Technology Co., Ltd.), 2-ethoxyphenol (98%, Macklin), 2-propoxyphenol (97%, Shanghai Bide Pharmaceutical Technology Co., Ltd.).

2.2 Catalyst preparation

Four γ-Al_2O_3-supported Ru catalysts with the same amount of Ru loading but varying Ru particle sizes were prepared by different methods. γ-Al_2O_3 (99.99%, Hangzhou Shuangmu Chemical Co., Ltd., S_{BET} = 153.6 m^2 g^{-1}) was used as the support.

The first catalyst (denoted as $Ru_{0.6}$/γ-Al_2O_3) was prepared by the deposition–precipitation (DP) method.[30,31] In a typical synthesis, 1.0 g of γ-Al_2O_3 was dispersed in 50 mL of deionized water in a 100 mL flask under magnetic stirring for 30 min. Then, 1.33 mL of an aqueous solution of ruthenium nitrosyl nitrate ($RuNO(NO_3)_3$, 15 mg mL^{-1}) was introduced into the γ-Al_2O_3 suspension and stirred for 30 min at room temperature. Subsequently, a designated amount of urea ($CO(NH_2)_2$) with a molar ratio of Ru to urea of 1 : 200 was added as a precipitation agent. The mixture was reacted at 80 °C for 8 h and subsequently aged at room temperature for 12 h under continuous stirring. The $Ru_{0.6}$/γ-Al_2O_3 precursor was obtained by filtration, washed several times with deionized water, and dried overnight at 80 °C.

The second catalyst (denoted as $Ru_{1.5}$/γ-Al_2O_3) was prepared by the liquid phase reduction method.[32,33] In a typical synthesis, 1.0 g of γ-Al_2O_3 was dispersed in 50 mL of deionized water under magnetic stirring for 1 h. A suspension of γ-Al_2O_3 was added dropwise to the metal solution under constant stirring for 2 h. A designated amount of sodium citrate with a stochiometric ratio of 1 : 3 (the moles of Ru/the moles of sodium citrate = 1 : 3) was added and stirred for another 0.5 h. Subsequently, the mixture was slowly added to the freshly prepared solution of $NaBH_4$ (the moles of Ru/the moles of $NaBH_4$ = 1 : 5, 10 g L^{-1}) and stirred for 12 h. The $Ru_{1.5}$/γ-Al_2O_3 precursor was obtained by centrifugation, washed several times with deionized water and absolute ethanol, and dried overnight in an oven at 60 °C.

The third catalyst (denoted as $Ru_{2.5}$/γ-Al_2O_3) was synthesized by a similar procedure to the $Ru_{1.5}$/γ-Al_2O_3 catalyst, except that sodium citrate was not added.

The fourth catalyst (denoted as $Ru_{7.5}$/γ-Al_2O_3) was prepared by the deposition precipitation method.[34,35] In a typical synthesis, 1.0 g of γ-Al_2O_3 was dispersed in 50 mL of deionized water and the pH was adjusted to 10.0 by dropwise addition of Na_2CO_3 (0.1 M). Then a designated amount of ruthenium trichloride was added to deionized water under vigorous stirring. In the meantime, the pH was controlled at 10.0. The mixture was stirred for 3 h at 50 °C, after which the suspension was cooled to room temperature. Washing five times with deionized water and filtering obtained the solid

and then the solid sample was dried at 100 °C overnight. The obtained solid powder was calcined in air at 400 °C for 2 h.

2.3 Catalyst characterization

Inductively coupled plasma-optical emission spectroscopy (ICP-OES). Weigh a certain amount of sample in a PTFE container, add 5 mL of concentrated nitric acid, 3 mL HCl, 1 mL HF, and 2 mL H_2O_2, seal it in a microwave digestion furnace, heat it at 1200 W for 20 min to 130 °C, keep it for 5 min, heat it for 20 min to 180 °C, keep it for 40 min, and then cool it to room temperature. Transfer the cooled solution to a 25 mL plastic volumetric flask. Finally, deionized water was used to fix the volume, the dissolved solution was tested successively, and the dilution beyond the curve range was tested again. The standard solution is a national standard substance, and the curve concentration points are 0, 0.5, 1.0, 2.0, and 5.0 mg L^{-1}.

N_2 adsorption–desorption measurements. A BSD-PS2 instrument was employed to perform N_2 physisorption tests. Before testing, samples were subjected to vacuum degassing at 200 °C for 4 h. Subsequently, N_2 adsorption–desorption tests were conducted under liquid nitrogen cooling conditions (−196 °C). The specific surface area and pore size distribution were determined using the Brunauer–Emmett–Teller (BET) method and the Barrett–Joyner–Halenda (BJH) desorption curve, respectively.

Transmission electron microscopy (TEM) and scanning transmission electron microscopy (STEM). TEM and STEM images, including elemental mappings were collected on an FEI-TEM instrument (Tecnai G2 F30 S-Twin) operated at 300 kV. Samples sparsely dispersed in ethanol were dropped on copper grids coated with amorphous carbon membranes and dried for TEM observations. The number-averaged particle size is calculated by $d = \sum n_i d_i / \sum n_i$, where n_i is the number of particles with size of d_i.

X-ray powder diffraction (XRD). A Rigaku SmartLab instrument was employed for conducting X-ray powder diffraction (XRD) testing, using a Cu-Kα excitation source with a scanning range from 2θ = 5–80°, a scanning speed of 5° min^{-1}, and a step size of 0.02. Phase analysis was performed by referring to standard powder diffraction cards, while the Scherrer equation was used to calculate the particle size of Ru.

X-ray photoelectron spectroscopy (XPS). The quasi-*in situ* XPS spectra of the activated samples were collected using an Axis Ultra Imaging Photoelectron Spectrometer (Kratos Analytical). The activated samples were transferred from the glove box directly into the ultrahigh vacuum chamber without exposure to air for XPS measurement at room temperature. The XPS spectra were processed using CasaXPS software. All the peaks were corrected by the carbon peak at 284.8 eV.

CO pulse chemisorption. The 50 mg catalyst was reduced at 200 °C for 2 h (heating rate: 10 °C min^{-1}) in 10% H_2/Ar gas (40 mL min^{-1}) atmosphere, purged with Ar for 0.5 h (40 mL min^{-1}) at 200 °C, and then cooled to 25 °C with CO pulses.

***In situ* DRIFTS.** *In situ* DRIFTS was conducted on a Bruker Equinox 55 instrument equipped with a mercury cadmium telluride (MCT) detector. For the CO adsorption procedure, Ru-based catalysts were treated *in situ* with a 20% H_2/Ar flow at 200 °C for 2 h and cooled to room temperature (25 °C), the gas flow was switched to Ar and held for 30 min and the background spectrum was collected. Then, switch the gas to a 5% CO/Ar and hold until saturated adsorption. The system was then purged with Ar to remove the unadsorbed CO and collected the DRIFTS spectra of CO adsorption at room temperature (25 °C). For the guaiacol adsorption procedure, Ru-based catalysts were treated *in situ* with a 20% H_2/Ar flow for 2 h at 200 °C and switched to pure Ar, heated to 250 °C then purged for 1 h. Then cool to 50 °C, hold for 30 min, and collect the background spectrum. Then open the valve of the pre-placed sample bottle of guaiacol and absorb guaiacol for 60 min, holding until saturated adsorption is reached. Finally, the system was purged with Ar for 60 min to remove unadsorbed guaiacol and the DRIFTS spectra of guaiacol adsorption were collected at 50 °C. For *in situ* DRIFTS of the guaiacol conversion procedure, Ru-based catalysts were treated *in situ* with a 20% H_2/Ar flow for 2 h at 200 °C and then switched to pure Ar purge for 30 min at 150 °C. After the purge, the background spectrum was collected. Then open the valve of the pre-placed guaiacol vial and absorb guaiacol for 60 min, holding until saturated adsorption is reached. The system was then purged with Ar for 60 min to remove unadsorbed guaiacol. Finally, switch the gas flow to 20% H_2 and collect DRIFTS spectra for 120 min.

2.4 Catalytic activity

The HDO reactions were carried out in a Teflon-lined stainless-steel reactor of 20 mL with a magnetic stirrer. Before the reaction, the catalyst was reduced at 200 °C for 2 h in flowing 10% H_2 (40 mL min^{-1}). In a typical procedure, 20 mg catalyst, 0.3 mmol guaiacol, and 3 mL H_2O were loaded into the reactor. The reactor was sealed and purged with N_2 six times to remove the air at room temperature and subsequently charged with H_2 (5 bar). Then the reactor was placed in a furnace at the desired reaction temperature. When the reactor reached the desired reaction temperature, the stirrer was started with a stirring speed of 400 rpm, and the reaction time was recorded.

Gas chromatography. The reaction mixture in the reactor was filtered and the liquid products were analyzed with a gas chromatograph (Agilent GC-8860) equipped with a flame ionization detector (FID) and an INNOWAX capillary column (0.32 mm in diameter, 30 m in length). 1,4-Dioxane was used as the internal standard to determine the conversion of substrates, selectivity and yield of the products. The carbon balances for the reactions were calculated using $C_{6\text{-membered ring}}$ balance which is given relative to the 6-membered ring products. The $C_{6\text{-membered ring}}$ balances for the reaction are 100 ± 5%.

The conversion of guaiacol ($X_{Guaiacol}$) and the yield of products are determined by:

$$X_G\ (\%) = \frac{G_{feed}\ (mol) - G_{residue}\ (mol)}{G_{feed}\ (mol)} \times 100\% \quad (1)$$

$$S\,(\%) = \frac{\text{Product}_i\,(\text{mol})}{G_{\text{feed}}\,(\text{mol}) - G_{\text{residue}}\,(\text{mol})} \times 100\% \quad (2)$$

$$\text{Yield}_{\text{product}}\,(\%) = \frac{\text{Product}\,(\text{mol})}{G_{\text{feed}}\,(\text{mol})} \times 100\% \quad (3)$$

$$\text{TO F} = \frac{\text{Product}\,(\text{mol})}{\frac{m_{\text{Cat.}} \times w_{\text{Ru}} \times D_{\text{Ru}}\,(\%)}{M_{\text{Ru}}} \times t}\ \left(\text{mol mol}_{\text{Ru}}{}^{-1}\ \text{s}^{-1}\right) \quad (4)$$

where X_G represents the conversion of guaiacol, G_{feed} represents the molar amount of guaiacol added, $G_{residue}$ represents the remaining molar amount of guaiacol, $Product_i$ (mol) represents the amount of $Product_i$ produced, $Yield_{product}$ represents the yield of the product, TOF represents the turnover frequency, m_{cat} represents the mass of the catalyst, w_{Ru} represents the load of metal, M_{Ru} represents the relative atomic mass of ruthenium, t represents the time, and D_{Ru} represents the dispersion of ruthenium.

3. Results and discussion

3.1 Catalyst characterization

Ru/γ-Al_2O_3 catalysts with varied average Ru particle sizes were prepared using different preparation procedures (as described in section 2) to investigate the size effect of the Ru particles on the HDO performance of guaiacol. ICP-OES results show that the Ru loading of each catalyst is ~1.5 wt% (Table 1). The texture properties of the catalysts prepared with different methods have little differences in surface area (Fig. S1,† Table 1). Fig. 1a–d and S2† display the representative TEM and STEM images of different Ru/γ-Al_2O_3 catalysts. It is shown that the average Ru particle sizes are 0.6 ± 0.1, 1.5 ± 0.2, 2.5 ± 0.3, and 7.5 ± 1.7 nm for $Ru_{0.6}$/γ-Al_2O_3, $Ru_{1.5}$/γ-Al_2O_3, $Ru_{2.5}$/γ-Al_2O_3, and $Ru_{7.5}$/γ-Al_2O_3, respectively. The Ru particle size distributions determined by CO chemisorption are close to the values from TEM (Table 1). The high-resolution TEM image shows that the lattice spacings of Ru particles in $Ru_{1.5}$/γ-Al_2O_3 (Fig. S3†) are 0.232 nm, corresponding to the (100) plane of Ru.[36,37] Except for the diffraction peaks related to the γ-Al_2O_3 support, no apparent peak of metallic Ru is observed in the XRD patterns of $Ru_{0.6}$/γ-Al_2O_3, $Ru_{1.5}$/γ-Al_2O_3, and $Ru_{2.5}$/γ-Al_2O_3 catalysts (Fig. 2a), suggesting the high dispersion of Ru on γ-Al_2O_3. The $Ru_{7.5}$/γ-Al_2O_3 catalyst shows diffraction peaks at 2θ of 41.9° and 44.1°, which are assigned to the hexagonal metallic Ru. The results consistently demonstrate that Ru/γ-Al_2O_3 catalysts with varying Ru particle sizes were successfully prepared.

Quasi-*in situ* X-ray photoelectron spectroscopy (XPS) was carried out to probe the chemical states of Ru, and Fig. S4† presents the Ru 3d and C 1s spectroscopy of Ru/γ-Al_2O_3 catalysts after pre-reduction. The Ru 3d XPS profiles exhibited both metallic (Ru^0) and oxidized ($Ru^{\delta+}$) states, in which oxidized states mainly locate at Ru–γ-Al_2O_3 interfaces. It was found that the $Ru^{\delta+}/Ru^0$ ratio significantly increased from $Ru_{7.5}$/γ-Al_2O_3 to $Ru_{0.6}$/γ-Al_2O_3, indicating increased interfacial contacts, in other words the dispersion of Ru increased.[38] The surface sites of the catalysts were further investigated by CO-DRIFTS at 25 °C (Fig. 2b and c and Table S1†). For $Ru_{0.6}$/γ-Al_2O_3, the peak at 2081 cm^{-1} was attributed to multi-carbonyl-adsorption modes of CO on Ru sites with low coordination numbers ($Ru–(CO)_x$, x = 2, 3), and the modes also appeared at 2072 cm^{-1} for $Ru_{1.5}$/γ-Al_2O_3. Broad peaks from 2000 to 2050 cm^{-1} were observed on four Ru/γ-Al_2O_3 catalysts, which were attributed top-absorption modes of CO on Ru NPs (Ru–CO).[39,40] In addition, the peaks at ~2125 cm^{-1} corresponded to Ru nanoclusters ($Ru^{\delta+}$–CO) at the Ru–γ-Al_2O_3 interface.[41] It is worth noting that the $Ru–(CO)_x$ mode on low coordinated Ru sites decreased with increased particle sizes, while it almost disappeared on $Ru_{7.5}$/γ-Al_2O_3. In contrast, top-absorption modes of Ru–CO on coordination saturated sites can hardly be observed on $Ru_{0.6}$/γ-Al_2O_3 with small Ru particle size. These results mean that the proportion of low coordinated surface atoms and coordination saturated atoms could be successfully controlled by regulating Ru particle size.

3.2 Effect of Ru particle size on catalytic performance

Catalytic HDO of guaiacol over Ru/γ-Al_2O_3 catalysts was performed in a batch reactor. Products such as phenol, cyclohexanone, cyclohexanol, and 2-MCH were monitored (Fig. 3a). The conversion of guaiacol on different Ru/γ-Al_2O_3 catalysts is compared in Fig. 3b. After 6 h, the conversion of guaiacol is ~5% on the $Ru_{0.6}$/γ-Al_2O_3 catalyst at 190 °C and 5 bar H_2, while $Ru_{1.5}$/γ-Al_2O_3 to $Ru_{7.5}$/γ-Al_2O_3 catalysts managed to convert 98.5, 86.8, and 82.1% of the substrate, respectively. The

Table 1 Physicochemical properties of the Ru/γ-Al_2O_3 catalysts

Catalyst	Ru[a] (wt%)	S_{BET} ($m^2\ g^{-1}$)	d_{XRD}[b] (nm)	d_{TEM} (nm)	Chemically absorbed CO[c] (mol of CO per mol of Ru)	$d_{CO\ chemisorption}$[d] (nm)
$Ru_{0.6}$/γ-Al_2O_3	1.58	165.9	—	0.6 ± 0.1	1.263	0.84
$Ru_{1.5}$/γ-Al_2O_3	1.50	159.1	—	1.5 ± 0.2	0.984	1.09
$Ru_{2.5}$/γ-Al_2O_3	1.57	172.8	—	2.5 ± 0.3	0.519	2.06
$Ru_{7.5}$/γ-Al_2O_3	1.49	157.9	9.5	7.5 ± 1.7	0.134	7.96

[a] Measured by inductive coupled plasma-optical emission spectroscopy (ICP-OES) on a Varian ICP-OES 720. [b] Calculated by the Scherrer equation. [c] Calculated based on the CO chemisorption data from BELCAT-B. [d] Calculated by an empirical relationship between the particle distribution (D) and the mean particle size (d), *i.e.*, $d = 1.07/D \times 100\%$.

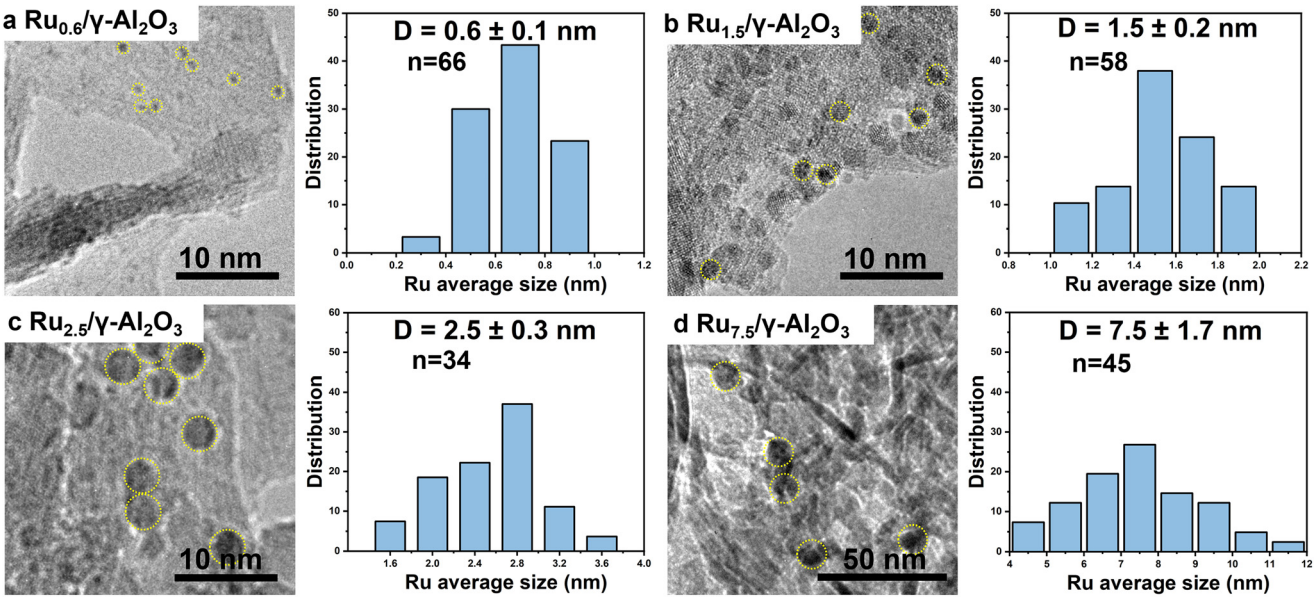

Fig. 1 TEM images and statistics particle size distribution bar charts of Ru/γ-Al_2O_3 catalysts with different Ru particle sizes. a. $Ru_{0.6}$/γ-Al_2O_3; b. $Ru_{1.5}$/γ-Al_2O_3; c. $Ru_{2.5}$/γ-Al_2O_3; d. $Ru_{7.5}$/γ-Al_2O_3 catalysts. All the catalysts were pre-reduced at 200 °C for 2 h.

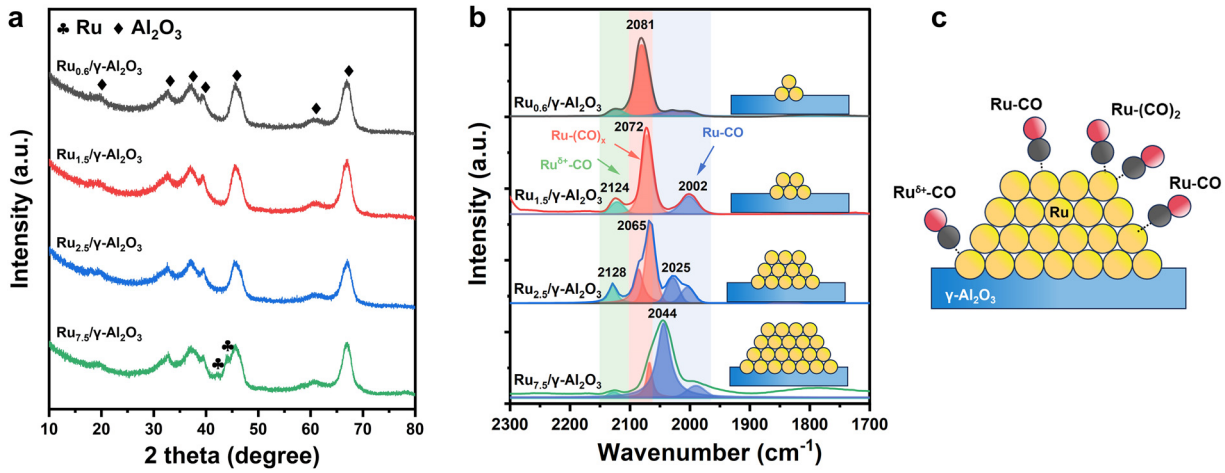

Fig. 2 a. XRD patterns of Ru/γ-Al_2O_3 catalysts (♣ represents Ru, ♦ represents Al_2O_3); b. CO-DRIFTS and fitting result of Ru/γ-Al_2O_3 catalysts; c. adsorption configurations of CO on Ru/γ-Al_2O_3 catalysts. All the catalysts are pre-reduced at 200 °C for 2 h.

conversion of guaiacol shows a volcanic trend with the increase of Ru particle size. Similarly, the selectivity to HDO products also shows a volcanic dependence on Ru particle size. Among all the catalysts, the $Ru_{1.5}$/γ-Al_2O_3 catalyst with 1.5 nm Ru shows the best catalytic performance, realizing ~95% yield of cyclohexanol during the reaction. This result suggests that the HDO of guaiacol on the Ru/γ-Al_2O_3 catalyst is a structure-sensitive reaction. The selectivity to products is strongly dependent on the particle size of Ru. The major product distribution as a function of reaction time on the $Ru_{1.5}$/γ-Al_2O_3 catalyst is exhibited in Fig. 3c. It is observed that the yield of cyclohexanol increases gradually with the extension of reaction time, whereas the yield of phenol and cyclohexanone increases firstly after declines, which indicates that phenol and cyclohexanone are the intermediates of guaiacol hydrogenation reaction. The yield of 2-MCH remains stable after reaching a maximum, which means that 2-MCH is difficult to further convert to cyclohexanol. The yield of the products of HDO of guaiacol over the $Ru_{7.5}$/γ-Al_2O_3 catalyst shows the same variation trend (Fig. 3d), but the final 2-MCH yield (~15%) exceeds that of $Ru_{1.5}$/γ-Al_2O_3 (~5%). In addition, the $Ru_{1.5}$/γ-Al_2O_3 catalyst shows excellent stability after 5 cycles at 190 °C and H_2 of 5 bar (Fig. S5 and Table S2†) and shows excellent HDO performance at lower temperature (150 °C) or lower H_2 pressure (3 bar) (Fig. S6 and S7†). As shown in Table S3,† the $Ru_{1.5}$/γ-Al_2O_3 catalyst is more competitive than the state-of-the-art Ru-based catalysts in terms of operating conditions and HDO reaction performance of guaiacol.

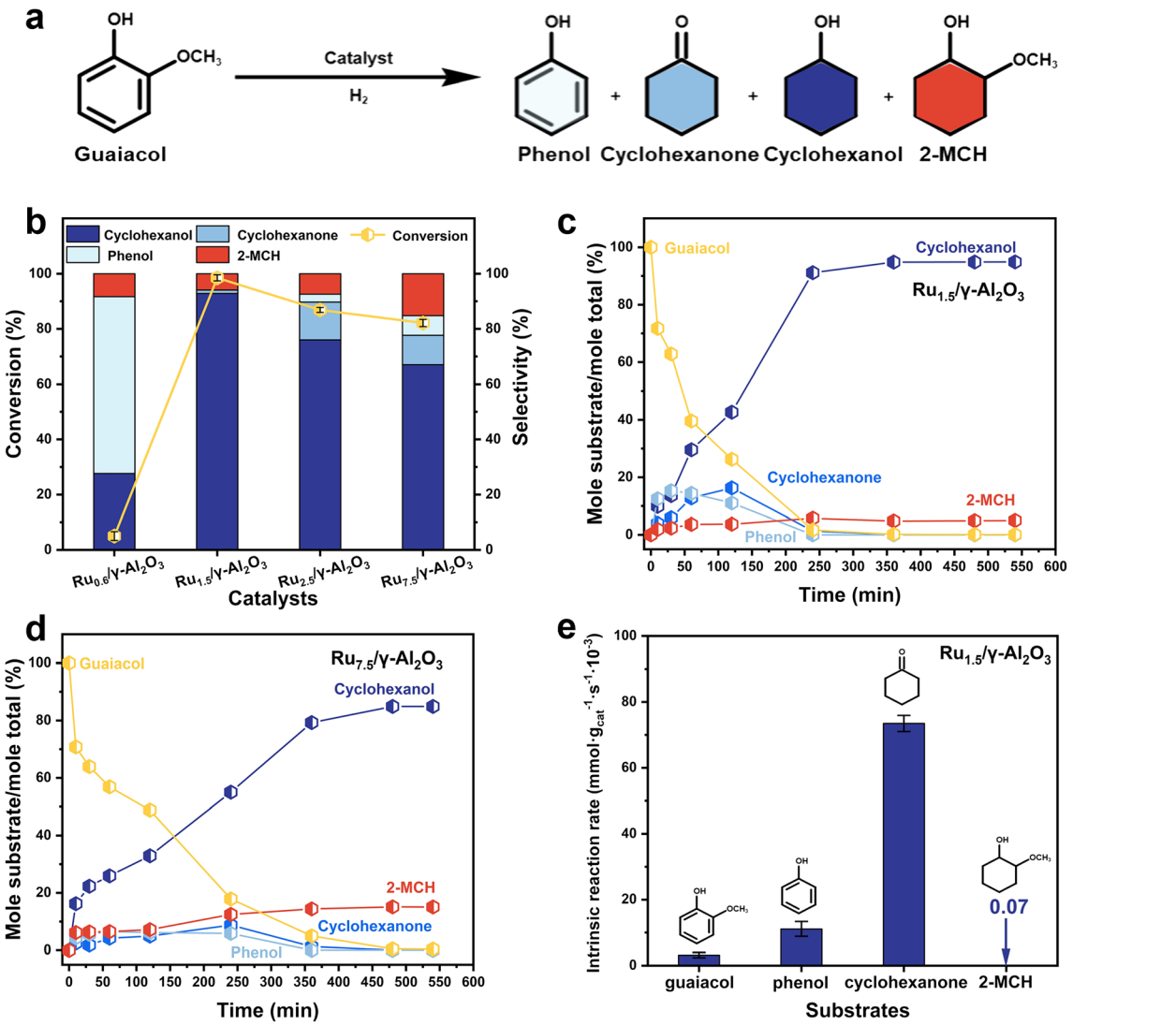

Fig. 3 a. The reaction formula of the guaiacol HDO reaction; b. guaiacol conversion and product selectivity of guaiacol hydrodeoxygenation over $Ru_{0.6}/\gamma\text{-}Al_2O_3$, $Ru_{1.5}/\gamma\text{-}Al_2O_3$, $Ru_{2.5}/\gamma\text{-}Al_2O_3$ and $Ru_{7.5}/\gamma\text{-}Al_2O_3$ catalysts (reaction conditions: 0.3 mmol guaiacol, 0.02 g catalyst, 3.0 mL H_2O, 5 bar H_2, 190 °C, 6 h, 400 rpm, the error bars show the deviation of guaiacol conversion based on three repeated experiments); c. time-dependent yield for HDO of guaiacol over the $Ru_{1.5}/\gamma\text{-}Al_2O_3$ catalyst; d. time-dependent yield for HDO of guaiacol over the $Ru_{7.5}/\gamma\text{-}Al_2O_3$ catalyst; e. initial reaction rate for guaiacol, phenol, cyclohexanone, and 2-MCH as substrates (conversion = 10 ± 5%) over the $Ru_{1.5}/\gamma\text{-}Al_2O_3$ catalyst, the error bars show the deviation of initial reaction rate conversion based on three repeated experiments.

To obtain better understanding on the reaction pathways, the intrinsic reaction rates on the $Ru_{1.5}/\gamma\text{-}Al_2O_3$ catalyst were tested in the kinetic region using phenol, cyclohexanone, and 2-MCH as the reaction substrates, respectively. As shown in Fig. 3e, cyclohexanol could be formed when guaiacol, phenol, or cyclohexanone is used as a substrate, and the reactivity order is as follows: cyclohexanone > phenol > guaiacol. In contrast, almost no cyclohexanol is detected when 2-MCH is used as a substrate. These results confirm that the demethoxylation of guaiacol is the most difficult step in the HDO process.

The reaction results infer that the HDO process of guaiacol follows two parallel pathways (Fig. 4a).[7,41] The priority of the two parallel reactions of C_{Ar}–OCH_3 bond cleavage (path I) and aromatic ring hydrogenation (path II) would determine the product distribution of the guaiacol HDO reaction. The initial selectivity to primary products at a low conversion level of ~15% is compared in Fig. 4b. 2-MCH shows a relatively high selectivity (31.14%) on large Ru particles of 7.5 nm ($Ru_{7.5}/\gamma\text{-}Al_2O_3$). Decreasing the Ru particle size to 0.6 nm ($Ru_{0.6}/\gamma\text{-}Al_2O_3$) leads to a significant decrease in the selectivity toward 2-MCH (8.69%), making it a minor reaction. Further, the intrinsic reaction rates of path I products (phenol, cyclohexanone, cyclohexanol) and path II products (2-MCH) are calculated, respectively. The sum of the intrinsic activities of path I products could be regarded as the C_{Ar}–OCH_3 bond cleavage rate ($r_{CAr-OCH_3}$) of guaiacol, and the intrinsic activity of the path II product could be regarded as the aromatic ring hydrogenation rate ($r_{C_{Ar}=C_{Ar}}$). As shown in Fig. 4c, the mass-specific intrinsic reaction rate of path I

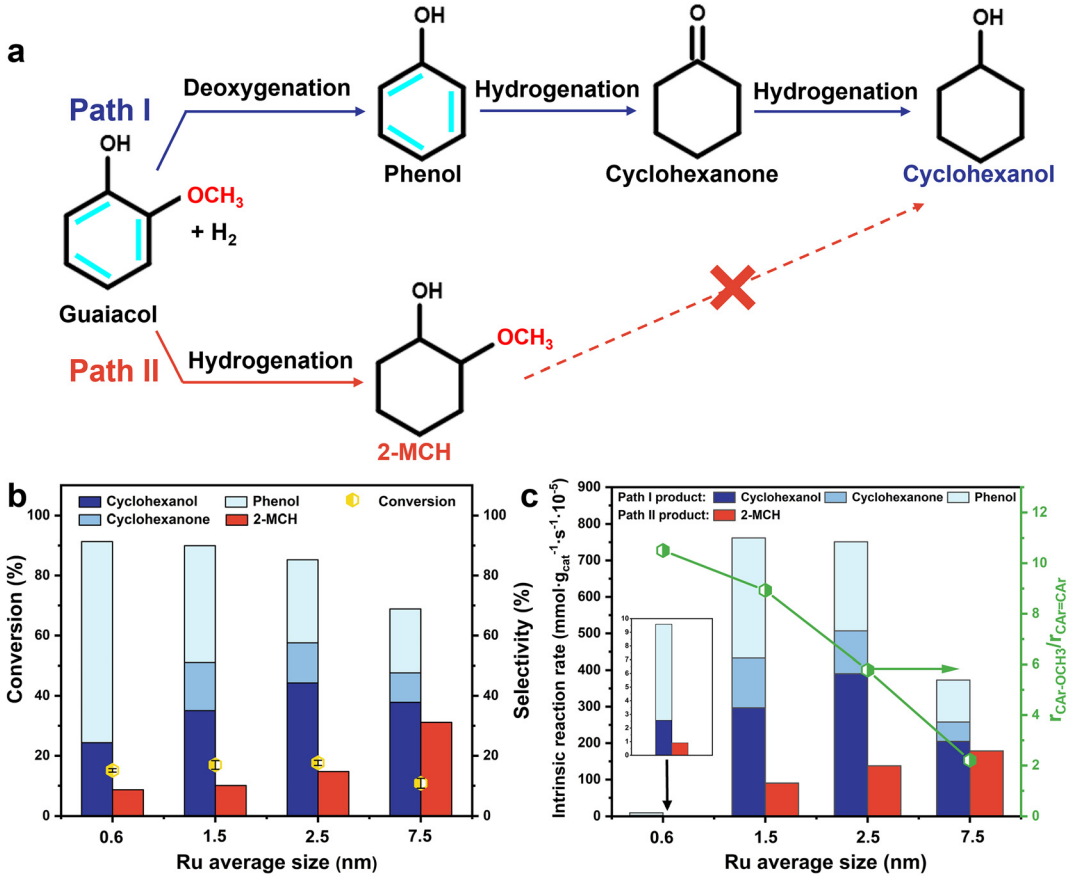

Fig. 4 a. Two estimated reaction pathways (guaiacol → phenol → cyclohexanone → cyclohexanol and guaiacol → 2-MCH) of HDO of guaiacol on the Ru/γ-Al_2O_3 catalysts; b. selectivity toward major products on catalysts with different Ru average sizes at ~15% guaiacol conversion (reaction conditions: 190 °C, 5 bar H_2, 3.0 mL H_2O, 0.3 mmol guaiacol, the error bars show the deviation of guaiacol conversion based on three repeated experiments); c. mass-specific intrinsic reaction rate of different products on Ru/γ-Al_2O_3 catalysts with different Ru particles and relative ratio of the CAr–OCH_3 bond cleavage rate ($r_{CAr-OCH_3}$) and aromatic ring hydrogenation rate ($r_{C_{Ar}=C_{Ar}}$) of guaiacol (reaction conditions of $Ru_{0.6}$/γ-Al_2O_3: 0.3 mmol guaiacol, 0.02 g catalyst, 3.0 mL H_2O, 5 bar H_2, 190 °C, 6 h, 400 rpm; reaction conditions of $Ru_{1.5}$/γ-Al_2O_3, $Ru_{2.5}$/γ-Al_2O_3 and $Ru_{7.5}$/γ-Al_2O_3: 0.3 mmol guaiacol, 0.01 g catalyst, 3.0 mL H_2O, 5 bar H_2, 190 °C, 1/6 h, 400 rpm).

products is ~10.5 times higher than that of the path II product for $Ru_{0.6}$/γ-Al_2O_3. Decreasing Ru particle size dramatically improves the $r_{CAr-OCH_3}$ and greatly inhibits the $r_{C_{Ar}=C_{Ar}}$ to 2-MCH. However, to achieve similar guaiacol conversion (~15%), the required reaction time for the $Ru_{0.6}$/γ-Al_2O_3 catalyst is ~36 times longer than that of the other three catalysts, resulting in a lower intrinsic reaction rate. H_2-TPD results prove that the H_2 adsorption capacity of the $Ru_{0.6}$/γ-Al_2O_3 catalyst is significantly decreased (Fig. S8†), which may cause the lack of hydrogen dissociation sites.[42] Consequently, the $Ru_{1.5}$/γ-Al_2O_3 catalyst with a Ru size of 1.5 nm shows the optimal performance for HDO of guaiacol to cyclohexanol.

Based on the mass-specific activity, the surface-specific activity normalized to the exposed Ru was also calculated. As shown in Fig. 5a, both pathways are more active when the Ru size grows larger; however, $r_{CAr-OCH_3}$ increases faster than $r_{C_{Ar}=C_{Ar}}$. Therefore, the ratio of $r_{C_{Ar}-OCH_3}/r_{C_{Ar}=C_{Ar}}$ decreases gradually when the particle size of Ru is increased. Such differences clearly indicate that varying Ru particle sizes remarkably changes the selectivity toward different reaction pathways. The catalytic performances of $Ru_{1.5}$/γ-Al_2O_3 and $Ru_{7.5}$/γ-Al_2O_3 were further evaluated at a low conversion level of ~15% at different temperatures (Fig. S9†). The process of C_{Ar}–OCH_3 bond cleavage is more sensitive to temperature than that of aromatic ring hydrogenation. It is found that $r_{CAr-OCH_3}$ increases faster than $r_{C_{Ar}=C_{Ar}}$ as the temperature increases on the $Ru_{1.5}$/γ-Al_2O_3 catalyst and the $r_{C_{Ar}-OCH_3}/r_{C_{Ar}=C_{Ar}}$ ratio of the $Ru_{1.5}$/γ-Al_2O_3 catalyst increases faster than that of $Ru_{7.5}$/γ-Al_2O_3 (Fig. 5b), which is the reason for the excellent cyclohexanol yield of the $Ru_{1.5}$/γ-Al_2O_3 catalyst.

3.3 Mechanistic investigation on adsorption and hydrodeoxygenation of guaiacol

To monitor the evolution of guaiacol over the $Ru_{1.5}$/γ-Al_2O_3 catalyst, *in situ* DRIFTS characterization was carried out. First, guaiacol was adsorbed on γ-Al_2O_3 and the $Ru_{1.5}$/γ-Al_2O_3 catalyst at 50 °C to confirm the characteristic bands of the reactant (Fig. S9†). Band deviations of guaiacol were found

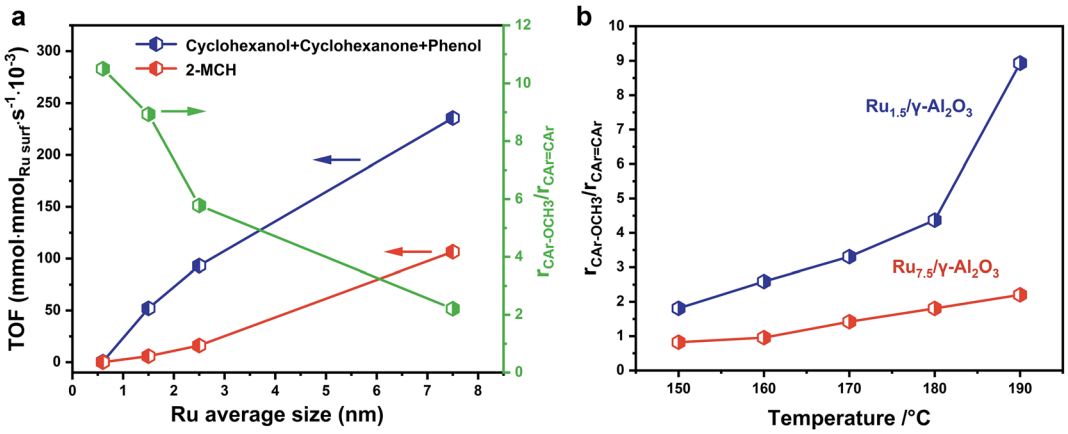

Fig. 5 a. The surface molar$_{Ru}$-specific activity (turnover frequency, TOF) as a function of Ru particle size and the relative ratio of $r_{CAr-OCH_3}$ and $r_{C_{Ar}=C_{Ar}}$ of guaiacol; b. the $r_{C_{Ar}-OCH_3}/r_{C_{Ar}=C_{Ar}}$ of Ru$_{1.5}$/γ-Al$_2$O$_3$ and Ru$_{7.5}$/γ-Al$_2$O$_3$ as a function of temperature.

between γ-Al$_2$O$_3$ and the Ru$_{1.5}$/γ-Al$_2$O$_3$ catalyst, which might be due to a change of adsorption site on metallic Ru NPs. The characteristic $\nu(C_{Ar}{=}C_{Ar})$ (1597, 1506 cm^{-1}), $\nu(C_{Ar}{-}OH)$ (1261 cm^{-1}), and $\nu(C_{Ar}{-}OCH_3)$ (1223 cm^{-1}) bands are related to adsorbed guaiacol (Fig. S10† and Table 2). Guaiacol was injected by Ar until adsorption saturation, then the gas was switched to H$_2$ at 150 °C (Fig. 6a). As shown in Fig. 6b and c, the band at 1221 cm^{-1}, which relates to the stretching vibration of the aromatic C–O(CH$_3$) bond [$\nu(C_{Ar}{-}OCH_3)$], disappears quickly. Meanwhile, the deformation/stretching vibrations of methyl [$\delta(CH_3)$ and $\nu(CH_3)$] located at 1448 and 2841 cm^{-1} gradually disappear, which verifies the dissociation of the methoxy group over the Ru$_{1.5}$/γ-Al$_2$O$_3$ catalyst. The bands at 1597 and 1505 cm^{-1}, which relate to the stretching vibration of the aromatic ring [$\nu(C_{Ar}{=}C_{Ar})$] of guaiacol, disappear gradually together with the stretching vibrations of the aromatic C–H bonds [$\nu(C_{Ar}{-}H)$] at 3066 cm^{-1} (Fig. 6b and S11†). Meanwhile, the series of bands at 2934 and 2860 cm^{-1} concerning the stretching vibration of the aliphatic C–H bonds in the CH$_2$ species [$\nu(CH_2)$] on the saturated ring of cyclohexanol gradually increase, indicating the efficient formation of cyclohexanol on the Ru$_{1.5}$/γ-Al$_2$O$_3$ catalyst. The band at 1260 cm^{-1} assigned to the stretching vibration of the aromatic C–O(H) bond [$\nu(C_{Ar}{-}OH)$] on the aromatic ring decreases progressively, proving similarly the hydrogenation capability of the Ru$_{1.5}$/γ-Al$_2$O$_3$ catalyst on the aromatic ring. It is worth noting that the decrease rate of the band at 1260 cm^{-1} is significantly faster than that of the band at 1221 cm^{-1} (Fig. 6c), indicating that C_{Ar}–O(R) bond cleavage takes place preferentially over aromatic ring hydrogenation.

To extend the understanding on the transformation rate of the aromatic ring and methoxy group, the intensity changes of the typical peaks of $\nu(C_{Ar}{=}C_{Ar})$ and $\nu(C_{Ar}{-}OCH_3)$ *versus* reaction time over the Ru$_{1.5}$/γ-Al$_2$O$_3$ catalyst were recorded (Fig. 6d). The intensity of $\nu(C_{Ar}{-}OCH_3)$ reduces quickly and the methoxy group is consumed completely in the first 10 min. On the contrary, the intensity of $\nu(C_{Ar}{=}C_{Ar})$ decreases slowly on the Ru$_{1.5}$/γ-Al$_2$O$_3$ catalyst, and the remaining aromatic ring intermediate on the catalyst surface by the 10 min test is ~70% of its original intensity. These results indicate that the removal of methoxy is a quicker step on the Ru$_{1.5}$/γ-Al$_2$O$_3$ catalyst than the hydrogenation of the aromatic ring. Demethoxylation preferentially occurs on the Ru$_{1.5}$/γ-Al$_2$O$_3$ catalyst, rather than aromatic ring hydrogenation, resulting in the inhibition of path II, which promotes the highly selective formation of cyclohexanol *via* path I. In addition, C_{Ar}–O(R) bond cleavage and aromatic ring hydrogenation were also observed in the 10 min test on *in situ* DRIFTS results of Ru$_{7.5}$/γ-Al$_2$O$_3$ under the same test conditions (Fig. S12†). In contrast, these two processes are both very slow on the Ru$_{0.6}$/γ-Al$_2$O$_3$ catalyst (Fig. S12†), owing to the lack of hydrogen dissociation sites, which is consistent with the reaction and characterization results in Fig. 3b and S8.†

The effect of particle size on different reaction pathways could be related to the variation of concentrations of different surface sites, such as terrace, step (low coordinated Ru sites) and corner (coordination saturated sites). The proportion of low coordinated Ru sites was estimated based on the fitting peak area integral of CO-DRIFTS results (Table S1† and Fig. 2b). It is found that the relative ratio of $r_{C_{Ar}-OCH_3}/r_{C_{Ar}=C_{Ar}}$ of guaiacol displayed a significant and well-defined correlation with low coordinated Ru site proportion (Fig. S13†), indicating that the C–O cleavage preferentially occurred at the low coordinated Ru, while the hydrogenation of aromatic rings preferentially

Table 2 DRIFTS peak assignments for HDO of guaiacol

Frequency (cm^{-1})	Assignment	Ref.
3070–3064, 3002	$\nu(C_{Ar}{-}H)$	5, 43
2940, 2927, 2863	$\nu(CH_2)$	5, 39
2846–2841	$\nu(CH_3)$	5, 43
1598–1594, 1508–1505	$\nu(C_{Ar}{=}C_{Ar})$	5, 40, 44, 45
1457–1454	$\delta(CH_3)$	5, 40, 44, 45
1351	$\delta(OH)$	5, 40, 44, 45
1263–1256	$\nu(C_{Ar}{-}OH)$	5, 40
1223–1220	$\nu(C_{Ar}{-}OCH_3)$	5, 40
1180	$\delta(C{-}H)$	5, 43
1104	$\nu(O{-}CH_3)$	43, 40

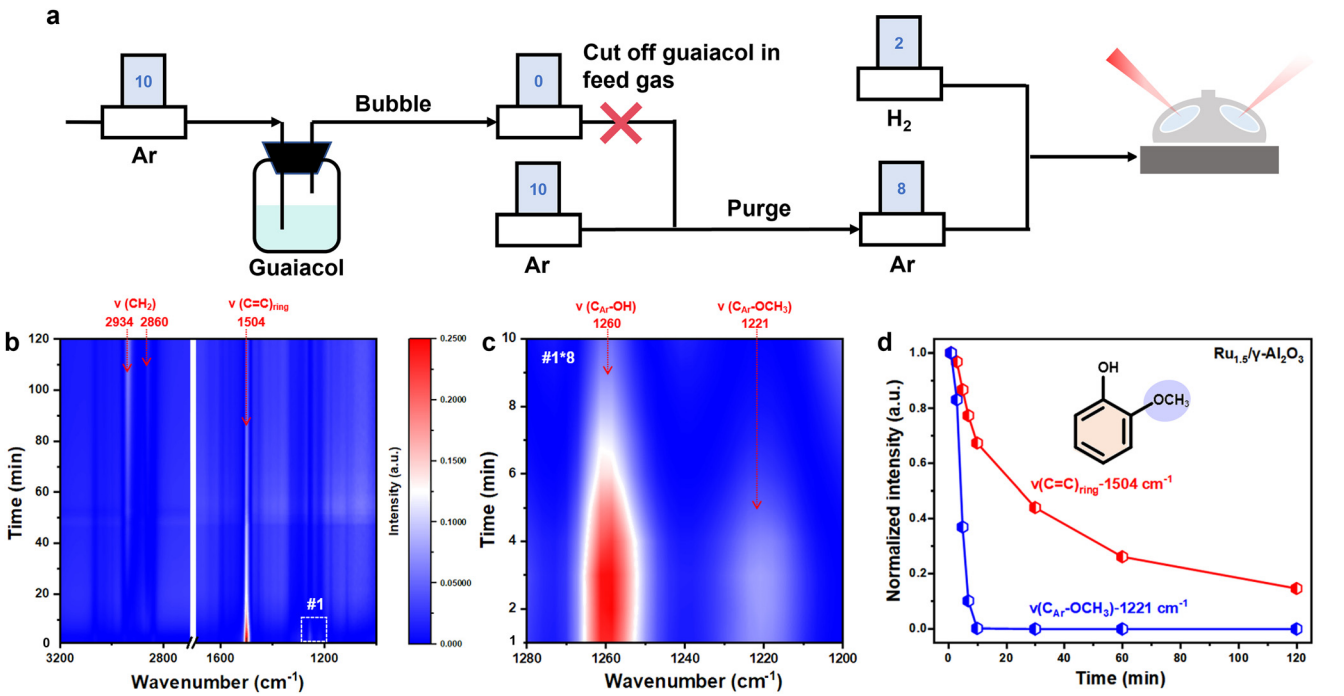

Fig. 6 a. Process diagram of *in situ* DRIFTS; b. *in situ* DRIFTS of the adsorbed intermediate hydrogenation on the $Ru_{1.5}/\gamma$-Al_2O_3 catalyst at 150 °C with the inlet gas switched from Ar to 20% H_2; c. partially enlarged detail of #1 in Fig. 6b; d. the normalized intensities of typical bands including $\nu(C_{Ar}{=}C_{Ar})$ at 1504 cm^{-1} and $\nu(C_{Ar}{-}OCH_3)$ at 1221 cm^{-1} *versus* reaction time over the $Ru_{1.5}/\gamma$-Al_2O_3 catalyst. The *in situ* reduced catalyst was first treated under Ar bubbling guaiacol vapor (10 mL min^{-1}) at 150 °C, 1 bar for 60 min, then the feed gas was changed to pure Ar (10 mL min^{-1}) for 60 min, and then the feed gas was changed from pure Ar to H_2 (2 mL min^{-1}) and Ar (8 mL min^{-1}) at 150 °C, 1 bar for another 120 min.

occurred at the coordination saturated Ru. Furthermore, the fractions of terrace, step, and corner atom numbers to the total surface Ru atom number in differently sized Ru/γ-Al_2O_3 catalysts were estimated using a truncated hexagonal bipyramid structure model (Table S4†), as indicated in Fig. S14.†[46,47] Increasing Ru particle sizes, the faction of coordination saturated terrace sites increases while the density of corner sites decreases. The fraction of step sites increases first and then decreases. The variation of step site density with particle size is consistent with the variation trend of mass-specific intrinsic reaction rate of C_{Ar}–O(R) bond cleavage (Fig. 4c); in contrast, the variation trend of terrace sites is consistent with the variation trend of mass-specific intrinsic reaction rate of aromatic ring hydrogenation, indicating that the step site is probably the active site for path I, while the terrace site is the active site for path II. The $Ru_{1.5}/\gamma$-Al_2O_3 catalyst with the highest low coordinated step site density in theory displays the highest product selectivity to cyclohexanol.

3.4 Evaluation of the selective HDO performance of the $Ru_{1.5}/\gamma$-Al_2O_3 catalyst to lignin-derived phenolic compounds

Other lignin-derived phenolic compounds were also tested to evaluate the catalytic HDO activity of the $Ru_{1.5}/\gamma$-Al_2O_3 catalyst (Table 3). It is observed that the isomers of guaiacol with methoxy substituted at the *meta* positions of the phenolic hydroxyl group could also achieve 98.5% yield of the cyclohexanol product over the $Ru_{1.5}/\gamma$-Al_2O_3 catalyst (Table 3, entry 1). The isomers of guaiacol with methoxy substituted at the *para* positions of the phenolic hydroxyl group could only achieve 80.0% yield of the cyclohexanol product (Table 3, entry 2). In addition, the alkyl-substituted guaiacol derivatives could obtain alkyl-substituted cyclohexanol products with substantial yields (Table 3, entries 3–5) over the $Ru_{1.5}/\gamma$-Al_2O_3 catalyst. Replacing the methoxy with other alkoxyl groups, such as ethoxy (Table 3, entry 6) and propoxy (Table 3, entry 7) groups, could also enable access to cyclohexanol with high yields of >90%.

Conclusions

In summary, we have demonstrated that HDO of guaiacol is a structure-sensitive reaction with a strong size effect over Ru/γ-Al_2O_3 catalysts. The γ-Al_2O_3 supported nanometer Ru particles at 1.5 nm showed the optimized performance (the cyclohexanol yield ~95% at 190 °C, 5 bar H_2). Decreasing the Ru particle size from 7.5 to 1.5 nm improves the intrinsic reaction rate of guaiacol by 1.6 times. Simultaneously, the C_{Ar}–OCH_3 bond cleavage rate improved by 2 times, while the aromatic ring hydrogenation rate decreased by 50%. Further decreasing the Ru particle size from 1.5 to 0.6 nm reduces the intrinsic reaction rate guaiacol by ~99%. The $r_{C_{Ar}-OCH_3}/r_{C_{Ar}=C_{Ar}}$ ratio increases with the decrease of Ru particle size. The size effect of Ru is due to the change of the density of low coordinated Ru sites to the coordination saturated sites with the particle diameters. The catalyst with 1.5 nm Ru has

Table 3 Diversification study of aromatic substrates with various substituents over the $Ru_{1.5}/\gamma\text{-}Al_2O_3$ catalyst

Entry	Substrate	Product	Yield (%)	Conv. (%)
1[a]	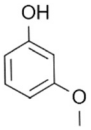		98.5	100.0
2[a]	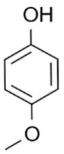	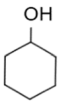	80.0	100.0
3[b]	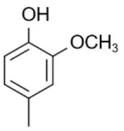	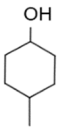	97.0	100.0
4[b]	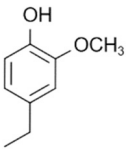	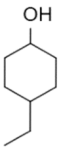	92.2	95.6
5[b]	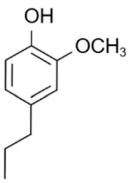	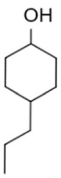	91.7	95.0
6[a]	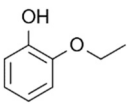	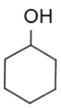	91.0	98.0
7[a]	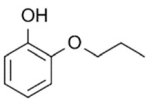	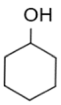	91.2	95.1

[a] Reaction conditions: substrate (0.3 mmol), $Ru_{1.5}/\gamma\text{-}Al_2O_3$ catalyst (0.02 g), H_2O (3.0 mL), 5 bar H_2, 190 °C, 6 h, and 400 rpm. [b] Reaction conditions: substrate (0.3 mmol), $Ru_{1.5}/\gamma\text{-}Al_2O_3$ catalyst (0.02 g), H_2O (3.0 mL), 5 bar H_2, 190 °C, 7 h, and 400 rpm.

been successfully applied to other lignin phenolic derivative monomers and still has excellent hydrodeoxygenation performance. The discovery is expected to design efficient and selective supported metal catalysts for converting lignin phenolic derivative monomers to high value-added chemicals under mild conditions.

Data availability

All data are available within the article and its ESI.†

Author contributions

The manuscript was written through the contributions of all authors. All authors have approved the final version of the manuscript.

Conflicts of interest

There are no conflicts to declare.

Acknowledgements

This work was financially supported by the Zhejiang Provincial Natural Science Foundation of China (LR22B030003, LQ24B030016), China Postdoctoral Science Foundation Grant (2022M712817) and Research and Development Program, Lianyungang Center of Institute for Molecular Engineering, PKU.

Notes and references

1 Y. Zhao, J. Zhan, R. Hu, G. Luo, J. Fan, J. H. Clark and S. Zhang, *Chem. Eng. J.*, 2024, **485**, 149934.
2 L. Wu, J. Wei, Y. Zhang, Y. He, X. Wang, H. Guo, Y. Tang and L. Tan, *Microporous Mesoporous Mater.*, 2023, **348**, 112347.
3 M. A. Kumar, N. Nagarjun, H. Manyar and P. Selvam, *ChemCatChem*, 2024, **16**, e202400578.
4 W. Zhang, W. Zhou, H. Lai, X. Ma and X. Zhang, *Chem. Eng. Sci.*, 2024, **291**, 119928.
5 K. Zhang, Q. Meng, H. Wu, J. Yan, X. Mei, P. An, L. Zheng, J. Zhang, M. He and B. Han, *J. Am. Chem. Soc.*, 2022, **144**, 20834–20846.
6 B. Zhang, Q. Meng, H. Liu and B. Han, *Acc. Chem. Res.*, 2023, **56**, 3558–3571.
7 G. Zasypalov, A. Vutolkina, V. Klimovsky, E. Abramov, V. Vinokurov and A. Glotov, *Appl. Catal., B*, 2024, **342**, 123425.
8 G.-Y. Xu, J.-H. Guo, Y.-C. Qu, Y. Zhang, Y. Fu and Q.-X. Guo, *Green Chem.*, 2016, **18**, 5510–5517.
9 W. Schutyser, S. Van den Bosch, J. Dijkmans, S. Turner, M. Meledina, G. Van Tendeloo, D. P. Debecker and B. F. Sels, *ChemSusChem*, 2015, **8**, 1805–1818.
10 Y. Nakagawa, M. Ishikawa, M. Tamura and K. Tomishige, *Green Chem.*, 2014, **16**, 2197–2203.
11 H. Zhou, H. Wang, A. D. Sadow and I. I. Slowing, *Appl. Catal., B*, 2020, **270**, 118890.
12 M. Zhang, L. Xiang, G. Fan, L. Yang and F. Li, *Mol. Catal.*, 2022, **533**, 112794.
13 Z. Wang, A. Wang, L. Yang, G. Fan and F. Li, *Mol. Catal.*, 2022, **528**, 112503.
14 M. I. Y. Nakagawa, M. Tamura and K. Tomishige, *Green Chem.*, 2014, **16**, 2197–2203.
15 D. Yin, R. Ji, F. Lv, L. Jiang, J. Zhang, M. Liu, Z. Jia, S. Yu, R. Zhao and Y. Liu, *Fuel*, 2023, **332**, 126060.
16 Y. Nakagawa, M. Ishikawa, M. Tamura and K. Tomishige, *Green Chem.*, 2014, **16**, 2197–2203.
17 J. Fu, J. Lym, W. Zheng, K. Alexopoulos, A. V. Mironenko, N. Li, J. A. Boscoboinik, D. Su, R. T. Weber and D. G. Vlachos, *Nat. Catal.*, 2020, **3**, 446–453.
18 T. S. Khan, D. Singh, P. P. Samal, S. Krishnamurty and P. L. Dhepe, *ACS Sustainable Chem. Eng.*, 2021, **9**, 14040–14050.
19 M. Ishikawa, M. Tamura, Y. Nakagawa and K. Tomishige, *Appl. Catal., B*, 2016, **182**, 193–203.
20 T. Liu, Z. Tian, W. Zhang, B. Luo, L. Lei, C. Wang, J. Liu, R. Shu and Y. Chen, *Fuel*, 2023, **339**, 126916.

21 X. Wang, M. Arai, Q. Wu, C. Zhang and F. Zhao, *Green Chem.*, 2020, **22**, 8140–8168.
22 X. Jia and W. An, *J. Phys. Chem. C*, 2018, **122**, 21897–21909.
23 J. Marlowe, P. C. Ford, M. M. Abu-Omar and P. Christopher, *Catal. Sci. Technol.*, 2023, **13**, 5662–5678.
24 F. Yang, D. Liu, Y. Zhao, H. Wang, J. Han, Q. Ge and X. Zhu, *ACS Catal.*, 2018, **8**, 1672–1682.
25 L. Dong, L.-L. Yin, Q. Xia, X. Liu, X.-Q. Gong and Y. Wang, *Catal. Sci. Technol.*, 2018, **8**, 735–745.
26 Y. Liu, X. Wu, Z. Li, J. Zhang, S.-X. Liu, S. Liu, L. Gu, L. R. Zheng, J. Li, D. Wang and Y. Li, *Nat. Commun.*, 2021, **12**, 4205.
27 R. Wu, Q. Meng, J. Yan, Z. Zhang, B. Chen, H. Liu, J. Tai, G. Zhang, L. Zheng, J. Zhang and B. Han, *Nat. Catal.*, 2024, **7**, 702–718.
28 C. Mondelli, G. Gözaydın, N. Yan and J. Pérez-Ramírez, *Chem. Soc. Rev.*, 2020, **49**, 3764–3782.
29 M. Peng, C. Li, Z. Wang, M. Wang, Q. Zhang, B. Xu, M. Li and D. Ma, *Chem. Rev.*, 2025, DOI: **10.1021/acs.chemrev.4c00618**.
30 J. Feng, L. Liu, X. Ju, M. Wang, X. Zhang, J. Wang and P. Chen, *ACS Sustainable Chem. Eng.*, 2022, **10**, 10181–10191.
31 X. Zhang, L. Liu, A. Wu, J. Zhu, R. Si, J. Guo, R. Chen, Q. Jiang, X. Ju, J. Feng, Z. Xiong, T. He and P. Chen, *ACS Catal.*, 2022, **12**, 2178–2190.
32 M. Tang, S. Mao, M. Li, Z. Wei, F. Xu, H. Li and Y. Wang, *ACS Catal.*, 2015, **5**, 3100–3107.
33 J. Shabir, C. Garkoti, P. Gupta, M. Sharma, S. Rani, M. Kumari and S. Mozumdar, *ACS Omega*, 2021, **6**, 1415–1425.
34 S. Fan, Z. Yao, W. Cheng, X. Zhou, Y. Xu, X. Qin, S. Yao, X. Liu, J. Wang, X. Li and L. Lin, *ACS Catal.*, 2023, **13**, 757–765.
35 Q. Wu, C. Shen, N. Rui, K. Sun and C.-j. Liu, *J. CO2 Util.*, 2021, **53**, 101720.
36 J. Zhang, H. Xiao, C. Du, X. Qin, S. Li, J. Sun, J. Fang and C. Zhang, *ACS Catal.*, 2022, **12**, 9812–9822.
37 A. K. Manal, G. V. Shanbhag and R. Srivastava, *Appl. Catal., B*, 2023, **338**, 123021.
38 J. Zhou, Z. Gao, G. Xiang, T. Zhai, Z. Liu, W. Zhao, X. Liang and L. Wang, *Nat. Commun.*, 2022, **13**, 327.
39 K. Hadjiivanov, J. C. Lavalley, J. Lamotte, L. Zhang, F. Maugé, J. Saint-Just and M. Che, *J. Catal.*, 1998, **176**, 415–425.
40 Y. Zhang, G. Fan, L. Yang, L. Zheng and F. Li, *ACS Sustainable Chem. Eng.*, 2021, **9**, 11604–11615.
41 J. Chen, Z. Ma, J. Qin, M. Chen, L. Dong, W. Mao, X. Zhou, Y. Long and J. Ma, *Fuel*, 2023, **353**, 129216.
42 B. Wang, P. Zhou, X. Yan, H. Li, H. Wu and Z. Zhang, *J. Energy Chem.*, 2023, **79**, 535–549.
43 E. V. Scoullos, M. S. Hofman, Y. Zheng, D. V. Potapenko, Z. Tang, S. G. Podkolzin and B. E. Koel, *J. Phys. Chem. C*, 2018, **122**, 29180–29189.
44 G. S. Foo, A. K. Rogers, M. M. Yung and C. Sievers, *ACS Catal.*, 2016, **6**, 1292–1307.
45 L. Huang, F. Tang, P. Liu, W. Xiong, S. Jia, F. Hao, Y. Lv and H. Luo, *Fuel*, 2022, **327**, 125115.
46 M. Ye, Y. Li, Z. Yang, C. Yao, W. Sun, X. Zhang, W. Chen, G. Qian, X. Duan, Y. Cao, L. Li, X. Zhou and J. Zhang, *Angew. Chem., Int. Ed.*, 2023, **62**, e202301024.
47 R. Van Hardeveld and F. Hartog, *Surf. Sci.*, 1969, **15**, 189–230.